Lattice dielectric properties of rutile math xmlns="http://www.w3.org/1998/Math/MathML">msub>mi >TiO/mi>mn>2/mn>/msub>/math>: First-principles anharmonic self-consistent phonon study

Tomohito Amano, Tamio Yamazaki, Ryosuke Akashi, Terumasa Tadano, and Shinji Tsuneyuki

Phys. Rev. B **107**, 094305 — Published 13 March 2023

DOI: 10.1103/PhysRevB.107.094305

Lattice dielectric properties of rutile TiO_2: First-principles anharmonic self-consistent phonon study

Tomohito Amano[1], Tamio Yamazaki[2], Ryosuke Akashi[1,3], Terumasa Tadano[4], and Shinji Tsuneyuki[1]
[1]*Department of Physics, The University of Tokyo, Hongo, Bunkyo-ku, Tokyo 113-0033, Japan*
[2]*JSR Corporation, RD Technology and Digital Transformation Center 1-9-2, Higashi-Shinbashi, Minato-ku, Tokyo 105-8640 Japan*
[3]*Quantum Materials and Applications Research Center, National Institutes for Quantum Science and Technology, 2-10, Ookayama, Meguro-ku, 152-0033, Tokyo, Japan and*
[4]*Research Center for Magnetic and Spintronic Materials, National Institute for Materials Science, Tsukuba 305-0047, Japan*
(Dated: February 17, 2023)

We calculate the lattice dielectric function of strongly anharmonic rutile TiO_2 from *ab initio* anharmonic lattice dynamics methods. Since an accurate calculation of the Γ point phonons is essential for determining optical properties, we employ the modified self-consistent approach, including third-order anharmonicity as well as fourth-order anharmonicity. The resulting optical phonon frequencies and linewidths at the Γ point much better agree with experimental measurements than those from a perturbative approach. We show that the four-phonon scattering process contributes as much as the third-order anharmonic term to phonon linewidths of some phonon modes. Furthermore, incorporating the frequency dependence of phonon linewidth reveals that experimentally known but unidentified peaks of the dielectric function are due to two-phonon process. This work emphasizes the importance of the self-consistent approach in predicting the optical properties of highly anharmonic materials.

I. INTRODUCTION

Titanium dioxide (TiO_2) is a polar semiconductor, which has been studied extensively from both experimental and theoretical perspectives for its phenomenal dielectric constants of 111 and 250 along the x and z axes, respectively. The consequent high refractive index is advantageous for various technological applications such as pigments and capacitors. Rutile TiO_2 thin film has also attracted attention as a high-κ dielectric material for DRAM [1].

The importance of rutile TiO_2 has instigated several experimental and theoretical studies on dielectric properties [2–11]. The large dielectric constant directly links to substantial Born effective charges and a low-frequency transverse optical phonon mode (A_{2u}, see Fig. 1). The frequency of the A_{2u} phonon rapidly increases with increasing temperature [12], as in the case of ferroelectric crystals, and is accompanied by a decrease in the static dielectric constant. However, unlike ferroelectric crystals, the frequency of the A_{2u} phonon does not become zero with lowering temperature, and therefore the system does not undergo a phase transition. Several perovskites (e.g., $KTaO_3$) are known as such materials and are called incipient ferroelectric. The strong anharmonicity of the lattice [6] is the reason for such remarkable temperature-dependent behavior. Gervais and Piriou [7, 8] applied the four-parameter semi-quantum model (FPSQ) as a model of the dielectric function and successfully fitted experimental reflectivity data. The model partially accounts for anharmonic effects employing different damping parameters for each transverse optical (TO) and longitudinal optical (LO) phonon. The FPSQ model studies [7–10] showed a marked difference in damping parameters between each LO and TO phonon, indicating that the conventional harmonic vibration model breaks down, especially for the A_{2u} phonon mode.

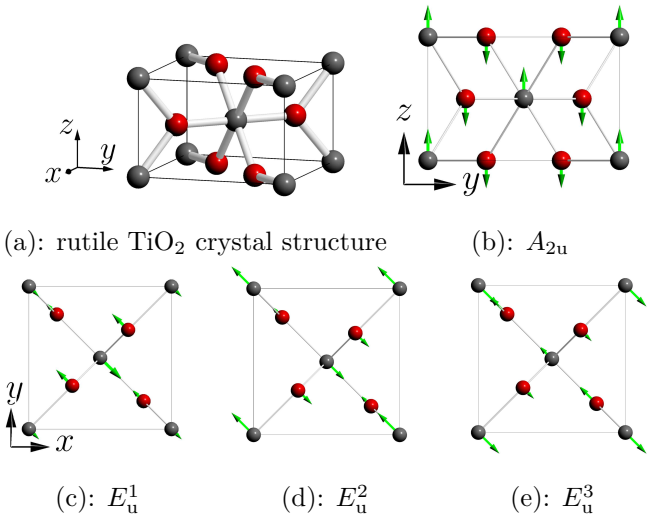

(a): rutile TiO_2 crystal structure (b): A_{2u} (c): E_u^1 (d): E_u^2 (e): E_u^3

FIG. 1: (a) The unit cell of rutile TiO_2, which contains two titanium atoms (black) and four oxygen atoms (red). (b-e) Schematic views of atomic displacements for the A_{2u} mode and the three E_u modes.

The first *ab initio* study on the lattice dynamics of rutile TiO_2 by Lee et al. [13] successfully calculated large Born effective charges and static dielectric constant, which led to many other studies on harmonic phonon

properties of rutile TiO_2 using input from first-principles calculations [14–21]. These calculations unveiled the importance of the mixed covalent and ionic bonding of s orbitals of oxygen and d orbitals of titanium, the cause of which is large polarizability due to long-range Coulomb interactions between the ions. The high Born effective charges could be caused by the dynamical transfer of electrons associated with atomic displacements. Therefore, careful convergence testing is required to get meaningful results. Also, the phonon frequencies of the A_{2u} and TA phonons show strong strain dependencies [15, 17, 20]. For example, the generalized gradient approximation (GGA) of Perdew-Burke-Ernzerhof yields an overestimation of the lattice constants, resulting in the A_{2u} phonon with imaginary frequency [14]. These results indicate that the phonon frequencies are sensitive to exchange-correlation functionals and the accuracy of the pseudopotentials [18]. While LDA functionals are often used in previous calculations and have been successful in describing lattice dynamics despite the underestimation of the lattice constants, recent works [18, 21] revealed that meta-GGA and hybrid functionals give us more accurate lattice constants.

Recently, an *ab initio* computational framework of phonon anharmonicity has been developed to calculate lattice thermal conductivity, phonon lifetime, and other phonon-related properties. In the framework, harmonic and anharmonic interatomic force constants (IFCs) are extracted from first-principles density functional theory (DFT) or density functional perturbation theory (DFPT) calculations. Computing a dynamical matrix from harmonic IFCs give us frequencies and eigenvectors of ordinary harmonic phonons, whereas anharmonic IFCs determine self-energies that cause the frequency shifts and linewidths.

Regarding rutile TiO_2, several previous studies [22, 23] have calculated thermal conductivity using this framework. Fu et al. [23] found that the finite-temperature effective IFCs [24], including higher order anharmonicity, are essential for predicting thermal conductivity, whereas calculations only including third-order anharmonicity underestimated the thermal conductivity. This result suggests that including higher-order IFCs explains the lattice properties of rutile TiO_2. The validity of perturbative approaches taken in previous studies is questionable in highly anharmonic cases such as rutile TiO_2, where the anharmonic term contributes as much as 20% of the A_{2u} phonon frequency at room temperature. The self-consistent phonon (SCPH) theory [25, 26], which includes the frequency shift associated with fourth-order anharmonicity in a self-consistent manner, can treat such strongly anharmonic crystals. Recently, the SCPH+B theory has been developed, including the frequency shift associated with third-order anharmonicity within a quasiparticle approximation [27]. It could describe the possible cancellation of frequency shifts of third and fourth-order anharmonicity in the A_{2u} phonon.

While the accurate SCPH theory has been successful in many thermal conductivity calculations, there have been few such attempts for lattice dielectric properties [28, 29], only discussing static dielectric constants. Perturbative approaches have been applied to lattice dielectric properties of weakly anharmonic materials. The Lorentz oscillator or FPSQ model studies revealed that the anharmonic term of four phonon scattering (4ph) is not negligible for calculating optical properties [30, 31]. Fugallo et al. [32] used the Cowley formula [33] to incorporate the frequency dependence of a damping parameter, and successfully obtained the dielectric spectra of MgO in good agreement with experiment. Here we aim to study the lattice dielectric properties of strongly anharmonic rutile TiO_2, where such a perturbative approach does not apply.

In this work, we perform first-principles lattice dynamics calculations to predict the IR optical properties of strongly anharmonic rutile TiO_2. The second-, third-, and fourth-order IFCs are computed using the least absolute shrinkage and selection operator (LASSO) technique based on first-principles calculations. Phonon frequency shifts and linewidths were calculated using SCPH+B, and the Cowley formula was utilized to calculate the dielectric function. We found that the results of the r^{2}SCAN functional are in good agreement with experimental measurements and that a self-consistent method is essential for describing the strong anharmonicity of the rutile TiO_2.

II. THEORY

A. Dielectric properties

The lattice dielectric function at photon energy $\hbar\omega$ is generally described by the classical Lorentz model

$$\epsilon(\omega) = \epsilon^{\infty} + \sum_j \frac{\Delta\epsilon_j \omega_{\mathbf{0}j}^2}{\omega^2 - \omega_{\mathbf{0}j}^2 + i\omega\gamma_{\mathbf{0}j}}, \tag{1}$$

where $\omega_{\boldsymbol{q}j}$, $\Delta\epsilon_j$, and $\gamma_{\boldsymbol{q}j}$ are the resonant frequency, the oscillator strength, and the damping (FWHM) of the phonon with wave vector $\boldsymbol{q}$ and mode j. ϵ^{∞} is the electronic dielectric constant. Although this model can describe dielectric properties qualitatively, it may not work well quantitatively because it is based on the Newton's equation of motion, ignoring the frequency dependence of damping constants.

According to the Maxwell's equations, the poles of a dielectric function are TO phonon frequencies, and the poles of a extinction coefficient $\eta = 1/\epsilon$ are LO phonon frequencies. The following factorized form was devised to analyze LO and TO phonons having different phonon frequencies and dampings. This model is called FPSQ, as there are four parameters per mode.

$$\epsilon(\omega) = \epsilon^{\infty} \prod_j \frac{\omega_{\mathbf{0}j,\mathrm{LO}}^2 - \omega^2 + i\omega\gamma_{\mathbf{0}j,\mathrm{LO}}}{\omega_{\mathbf{0}j,\mathrm{TO}}^2 - \omega^2 + i\omega\gamma_{\mathbf{0}j,\mathrm{TO}}}. \tag{2}$$

When LO-TO splitting is large, namely, $\omega_{\rm LO} \gg \omega_{\rm TO}$, the difference in a damping is more pronounced, and the FPSQ model is more suitable than the Lorentz model. Even though the model does not consider the frequency dependence of damping, it successfully explains the experimental values well for a wide range of materials.

On the other hand, Cowley [33] derived an equation incorporating the full frequency dependence of dampings using the anharmonic lattice dynamics theory [34] and the linear response theory (see Appendix A for derivation),

$$\epsilon_{\alpha\beta}(\omega) = \epsilon^{\infty}_{\alpha\beta} + \frac{1}{v_0}\sum_j \frac{S^j_{\alpha\beta}}{(\omega_{\mathbf{0}j})^2 - \omega^2 - 2\omega_{\mathbf{0}j}\Sigma_{\mathbf{0}j}(\omega)}, \quad (3)$$

where v_0 is the volume of the unitcell, α and β are Cartesian indices, and $\Sigma(\omega) = -\Delta\omega(\omega) + i\Gamma(\omega)$ is phonon self-energy, where $\Delta\omega(\omega)$ and $\Gamma(\omega)$ are called frequency shift and linewidth, respectively. Phonon lifetime $\tau_{\boldsymbol{q}j}$ is related to linewidth as $\tau_{\boldsymbol{q}j} = 1/2\Gamma(\omega_{\boldsymbol{q}j})$, and a damping parameter in the Lorentz model or the FPSQ model holds $\gamma_{\mathbf{0}j} = 2\Gamma(\omega_{\mathbf{0}j})$. Summations are taken only for TO phonons at the Γ point. S is called mode-oscillator strength defined as follows [35],

$$S^j_{\alpha\beta} = \left(\sum_{\kappa\alpha'} Z^*_{\kappa,\alpha\alpha'}\frac{e_{\kappa\alpha'}(\mathbf{0}j)}{\sqrt{m_\kappa}}\right)\left(\sum_{\kappa\beta'} Z^*_{\kappa,\beta\beta'}\frac{e_{\kappa\beta'}(\mathbf{0}j)}{\sqrt{m_\kappa}}\right), \quad (4)$$

where κ is the index of the atoms, Z^* is a Born effective charge, m_κ is the mass of the κ-th atom, and $e_{\alpha\kappa}(q)$ is a phonon eigenvector normalized as $\sum_{\kappa\alpha}\left[e_{\kappa\alpha}(\boldsymbol{q}j)\right]^* e_{\kappa\alpha}(\boldsymbol{q}j') = \delta_{jj'}$.

The reflectivity R of optical waves normal to the surface is given by

$$R(\omega) = \left|\frac{\sqrt{\epsilon(\omega)} - 1}{\sqrt{\epsilon(\omega)} + 1}\right|^2. \quad (5)$$

B. Phonon self-energy

Calculating a dielectric function from Eq. (3) requires estimating the phonon self-energy Σ. As the main contribution to the self-energy, we consider the following terms

$$\Sigma = \Sigma^{\rm T} + \Sigma^{\rm B} + \Sigma^{\rm L} + \Sigma^{\rm 4ph}. \quad (6)$$

Here, T, B, L, and 4ph stand for tadpole, bubble, loop, and four phonon scattering. Figure 2 depicts the Feynman diagrams of these self-energies. These diagrams are given by the following formulae [36].

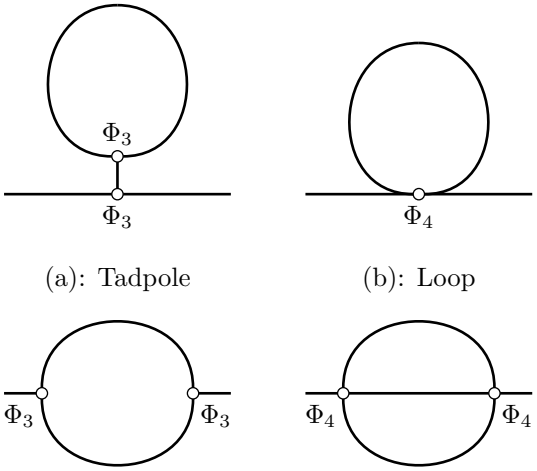

(a): Tadpole (b): Loop

(c): Bubble (d): 4ph

FIG. 2: Feynman diagrams of phonon self energies. Solid lines and open circles represent phonon propergators and phonon vertexes, respectively.

$$\Sigma^{\rm T}_q(\omega) = \frac{-1}{\hbar}\sum_{q_2,j_1=\rm TO} V(-q,q,\mathbf{0}j_1)V(\mathbf{0}j_1,q_2,-q_2)\frac{2n_2+1}{\omega_{\mathbf{0}j_1}} \quad (7)$$

$$\Sigma^{\rm B}_q(\omega) = \frac{1}{2\hbar}\sum_{q_1,q_2,s\pm1}|V(-q,q_1,q_2)|^2 \left[\frac{n_1+n_2+1}{s\omega_c+\omega_{q_1}+\omega_{q_2}} - \frac{n_1-n_2}{s\omega_c+\omega_{q_1}-\omega_{q_2}}\right] \quad (8)$$

$$\Sigma^{\rm L}_q(\omega) = -\sum_{q_1} V(q,-q,q_1,-q_1)\frac{2n_1+1}{2} \quad (9)$$

$$\Sigma^{\rm 4ph}_q(\omega) = \frac{1}{6\hbar}\sum_{q_1q_2q_3,s\pm1} V(-q,q_1,q_2,q_3)V(-q_1,-q_2,-q_3,q) \left[\frac{(n_1+1)(n_2+1)(n_3+1)-n_1n_2n_3}{s\omega_c+\omega_{q_1}+\omega_{q_2}+\omega_{q_3}} + \frac{3n_1(n_2+1)(n_3+1)-(n_1+1)n_2n_3}{s\omega_c-\omega_{q_1}+\omega_{q_2}+\omega_{q_3}}\right] \quad (10)$$

Here and in the following, we use q for the shorthand notation of $(\boldsymbol{q},j)$, satisfying $q=(\boldsymbol{q},j)$ and $-q=(-\boldsymbol{q},j)$. $n_i = n(\omega_{q_i}) = 1/(e^{\beta\hbar\omega_{q_i}}-1)$ is the BoseEinstein distribution function and $\omega_c = \omega + i0^+$ with 0^+ being a positive infinitesimal. In addition, the summation in Eq. (8) is restricted to the pairs $(\boldsymbol{q}_1,\boldsymbol{q}_2)$ satisfying the momentum conservation $\boldsymbol{q}_1+\boldsymbol{q}_2 = \boldsymbol{q}+\boldsymbol{G}$, where $\boldsymbol{G}$ is a reciprocal lattice vector. Similarly, the sum of the 4ph diagram (10) is limited to the pairs $(\boldsymbol{q}_1,\boldsymbol{q}_2,\boldsymbol{q}_3)$ satisfying $\boldsymbol{q}_1+\boldsymbol{q}_2+\boldsymbol{q}_3 = \boldsymbol{q}+\boldsymbol{G}$. $V(q_1,q_2,q_3)$ and $V(q_1,q_2,q_3,q_4)$

are three and four phonon scattering matrices defined as

$$V(q_1,q_2,q_3)=\frac{1}{N^{1/2}}\left(\frac{\hbar}{2}\right)^{3/2}\sum_{\substack{\kappa_1\mu_1\\ l_2\kappa_2\mu_2\\ l_3\kappa_3\mu_3}}\Phi^{0\kappa_1,l_2\kappa_2,l_3\kappa_3}_{\mu_1\mu_2\mu_3}\times\frac{e_{\kappa_1\mu_1}(q_1)e_{\kappa_2\mu_2}(q_2)e_{\kappa_3\mu_3}(q_3)}{\sqrt{m_{\kappa_1}m_{\kappa_2}m_{\kappa_3}}}e^{i(\boldsymbol{q}_2\cdot\boldsymbol{r}_2+\boldsymbol{q}_3\cdot\boldsymbol{r}_3)},\tag{11}$$

$$V(q_1,q_2,q_3,q_4)=\frac{1}{N}\left(\frac{\hbar}{2}\right)^{2}\sum_{\substack{\kappa_1\mu_1\\ l_2\kappa_2\mu_2\\ l_3\kappa_3\mu_3\\ l_4\kappa_4\mu_4}}\Phi^{0\kappa_1,l_2\kappa_2,l_3\kappa_3,l_4\kappa_4}_{\mu_1\mu_2\mu_3\mu_4}\times\frac{e_{\kappa_1\mu_1}(q_1)e_{\kappa_2\mu_2}(q_2)e_{\kappa_3\mu_3}(q_3)e_{\kappa_4\mu_4}(q_4)}{\sqrt{m_{\kappa_1}m_{\kappa_2}m_{\kappa_3}m_{\kappa_4}}}\times e^{i(\boldsymbol{q}_2\cdot\boldsymbol{r}_2+\boldsymbol{q}_3\cdot\boldsymbol{r}_3+\boldsymbol{q}_4\cdot\boldsymbol{r}_4)},\tag{12}$$

where μ is a Cartesian index, l is the index of unit cells, $\boldsymbol{r}_l$ is the position of the lth primitive cell, and Φ represents the third- and fourth-order IFCs, which is the derivative of the potential energy U with respect to atomic displacements u as follows,

$$\Phi^{l_1\kappa_1,\cdots,l_n\kappa_n}_{\mu_1\cdots\mu_n}=\frac{\partial U}{\partial u_{\mu_1}(l_1\kappa_1)\cdots\partial u_{\mu_n}(l_n\kappa_n)}.\tag{13}$$

The tadpole and loop diagrams are real constants, while the bubble and 4ph diagrams are complex numbers that depend on the frequency. Thus, only the bubble and 4ph diagrams contribute to phonon linewidths. We ignore the frequency shifts due to thermal expansion and isotope effect because they are small in rutile TiO_2 at room temperature [37].

As mentioned before, the anharmonicity of rutile TiO_2 is so strong that these self-energies must be treated in a self-consistent manner. Σ^{T} and Σ^{L} are considered self-consistently in the SCPH theory, and anharmonic phonon frequencies are obtained with solving the following self-consistent equation for ω.

$$\left[G^{\mathrm{S}}_q(\omega)\right]^{-1}=\left[G^{0}_q(\omega)\right]^{-1}-\Sigma^{\mathrm{T}}[G^{\mathrm{S}}]-\Sigma^{\mathrm{L}}[G^{\mathrm{S}}]\tag{14}$$

Here, G^0_q and G^{S}_q are harmonic and SCPH phonon Green's functions, respectively. We write the resultant SCPH frequencies as ω^{S}_q. The SCPH+bubble (SCPH+B) theory [27] has recently been proposed to consider Σ^{B} in the SCPH theory. After solving the SCPH equation (14), this method solves the following non-linear equation for Ω,

$$\Omega^2_q=\left(\omega^{\mathrm{S}}_q\right)^2-2\omega^{\mathrm{S}}_q\,\mathrm{Re}\,\Sigma^{\mathrm{B}}_q[G^{\mathrm{S}},\Phi_3](\omega=\Omega_q).\tag{15}$$

In the following, we write the SCPH+B phonon frequencies as $\Omega^{\mathrm{SCPH+B}}$.

After obtaining the anharmonic phonon frequencies and eigenvectors by the SCPH+B equation, the imaginary part of Σ^{B} and Σ^{4ph} are considered in a frequency-dependent form as

$$\Sigma^{\mathrm{B+4ph}}(\omega)=\mathrm{Im}\,\Sigma^{\mathrm{B}}[G^{\mathrm{SCPH+B}},\Phi_3](\omega)+\Sigma^{\mathrm{4ph}}[G^{\mathrm{SCPH+B}},\Phi_4](\omega).\tag{16}$$

We use not harmonic Green's functions but SCPH+B Green's functions to include the phonon frequencies renormalization effect. We finally obtain a dielectric function by substituting these self-energies into Eq. (3) as

$$\epsilon_{\alpha\beta}(\omega)=\epsilon^{\infty}_{\alpha\beta}+\frac{1}{v_0}\sum_j\frac{S^j_{\alpha\beta}}{\left(\Omega^{\mathrm{SCPH+B}}_{\mathbf{0}j}\right)^2-\omega^2-2\Omega^{\mathrm{SCPH+B}}_{\mathbf{0}j}\Sigma^{\mathrm{B+4ph}}(\omega)}.\tag{17}$$

All the parameters in Eq. (17) will be determined if second, third, and fourth-order IFCs are provided other than ϵ^{∞} and Z^*, which can be calculated from DFPT. As ϵ^{∞} is well known to be overestimated in DFT and the evaluation of ϵ^{∞} is outside the scope of our work, we use the experimental values [2] of $\epsilon^{\infty}_{xx}=5.91$ and $\epsilon^{\infty}_{zz}=7.20$ in the following calculations.

III. RESULTS AND DISCUSSION

A. Computational Details

The IFCs of rutile TiO_2 were calculated from *ab initio* calculations using VASP [38]. The local density approximation (LDA) [39] and the r^2 strongly constrained and appropriately normed (r^{2}SCAN) meta-GGA [40] with the projector augmented-wave method [41] were used for exchange and correlation functionals. We have also performed calculations with the PBEsol functional [42] to see how results changes due to functionals and the results are discussed in Sec. III E. The semicore $3s$ and $3p$ states are considered as the valence electrons in the Ti pseudopotential. The plane-wave energy and charge cutoffs are 800 eV and 1200 eV, respectively. The energy convergence threshold is set at 1×10^{-9} eV.

Before phonon calculations, the lattice parameter and geometry optimization was performed with the electronic sampling of a $10\times10\times10$ Monkhorst-Pack grid, which converged to the maximum error in forces of 1 meV/Å and stresses of 0.01 GPa. Born effective charges are obtained from DFPT calculations for both long-range interactions and dielectric properties.

We estimated IFCs via linear-regression optimization using DFT forces of various atomic configurations as training data. The harmonic terms were fitted from the finite displacement method with one atom moved by 0.01 Å, where the atomic forces were calculated building

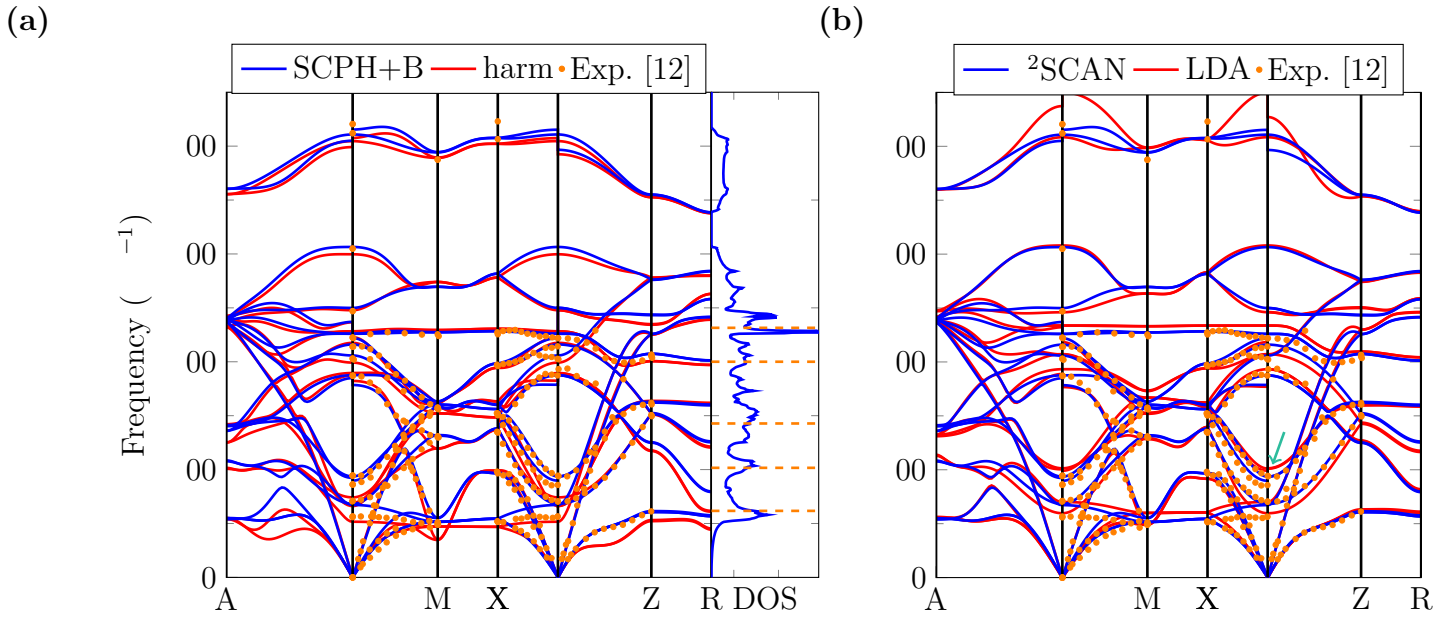

FIG. 3: (a) The harmonic (red) and SCPH+B (blue) band structures of r^{2}SCAN functional at 300K with the experimental values from inelastic neutron scattering (orange dot). The SCPH+B DOS is also illustrated at the same time. The orange dashed lines are the peak obtained from the inelastic neutron scattering experiment [43]. (b) The SCPH+B band structure with r^{2}SCAN (blue) and LDA (red) functional. The green arrow indicate the A_{2u} mode, which is overestimated in the LDA functional.

a $2 \times 2 \times 4$ supercell with a $5 \times 5 \times 5$ electronic wave vector grid. Then, we used the LASSO technique [44] to extract anharmonic IFCs from the 100 displacement-force training datasets with all atoms moved by 0.04 Å in random directions. When constructing the IFC model, we included all possible IFCs in a $2 \times 2 \times 4$ supercell for harmonic IFCs. The cubic, quartic, fifth, and sixth terms were considered with cutoffs of 15, 10, 5, and 5 bohr, respectively.

The SCPH and SCPH+B equations, including Σ^{L} and the real part of Σ^{B}, were solved for a $2 \times 2 \times 2$ q points, where a $6 \times 6 \times 6$ q points grid was used for computing the self-energies [25]. Σ^{T} is ommited because of it's smallness in rutile TiO_2. Finally, the imaginary parts of Σ^{B} and Σ^{4ph} are calculated with using a $15 \times 15 \times 15$ and $10 \times 10 \times 10$ q points grid, respectively. The extraction of IFCs, the lattice dynamics calculations, and the SCPH calculations were performed using the ALAMODE [45] package.

B. phonon frequencies

Rutile TiO_2 has a tetragonal unit cell and the $P4_2/mnm$ space group, as shown in Fig. 1. Because six atoms are in the unit cell, there are 15 optical phonon modes and three acoustic phonon modes. The optical phonons at the Γ point of the Brillouin zone belong to the following irreducible representations,

$$\Gamma_{\mathrm{opt}} = A_{1g} + A_{2g} + A_{2u} + 2B_{1u} + B_{1g} + B_{2g} + E_g + 3E_u. \quad (18)$$

Expressions with subscript g are Raman-active, those with u are infrared-active except for B_{1u}, while the representations with the E symbol are degenerate. E_u and A_{2u} are vibrations in the xy-plane and z-direction, respectively, contributing to the dielectric function's xy and z components. In the E_u^1 phonon, the softest E_u phonon, and the A_{2u} phonon, the Ti and O ions move in opposite directions, whereas in the E_u^2 and E_u^3 modes, the two Ti ions move in opposite directions, as in Fig. 1.

TABLE I: calculated lattice constants with LDA and r^{2}SCAN. Experimental values are taken from a neutron diffraction study [46]. a is the lattice constant in the x and y directions, and c in the z direction. v_0 is the lattice volume. The four oxygen O ions are located at the $(u, u, 0)$, $(1-u, 1-u, 0)$, $(1/2-u, 1/2+u, 1/2)$, and $(1/2+u, 1/2-u, 1/2)$ in the fractional coordinate, where u is a parameter.

	a (Å)	c (Å)	u	c/a	v_0 (Å^3)
LDA	4.552	2.922	0.3038	0.642	60.55
r^{2}SCAN	4.602	2.961	0.3046	0.643	62.71
Exp. 300 K [46]	4.593	2.959	0.3048	0.644	62.42
Exp. 15 K [46]	4.587	2.954	0.3047	0.644	62.15

We first present results for optimized lattice constants from LDA and r^{2}SCAN compared with experimental values at 15 K and 295 K in Table I. As in previous studies, LDA slightly underestimates the lattice constants by 0.8%. The r^{2}SCAN functional, a meta-GGA family, shows good agreement with experimental values within 0.4%, though the GGA-PBE functional is known to overestimate the lattice constants.

Table II shows that Born effective charges obtained from r^{2}SCAN are around 10% smaller than those from LDA. The LDA values agree well with those of previous LDA studies [13, 18, 49, 50]. Based on the LO phonon frequencies results discussed below, Born effective charges calculated from r^{2}SCAN are considered more accurate than those from LDA.

Figure 3 shows the phonon dispersion spectrum along the high-symmetry points in the first Brillouin zone at 300 K with non-analytic term correction. Figure 3a compares harmonic phonon frequencies (red, abbreviated as harm) with SCPH+B frequencies (blue) using the r^{2}SCAN functional, while Fig. 3b compares the SCPH+B frequencies using LDA (red) and r^{2}SCAN (blue), together with inelastic neutron scattering results from Traylor [12] (orange dots). Figure 3a also shows the density of states (DOS) of r^{2}SCAN and SCPH+B, with the orange dashed lines being the positions of the five DOS peaks observed in the neutron experiment by Lan and Fultz [51]. Overall, the combination of the r^{2}SCAN functional and the SCPH+B calculation agrees well with the experimental data except for the lowest optical phonon branch (B_{1u}), which is known to be sensitive to the choice of functionals [17]. The frequencies of the A_{2u} and E_u^1 phonons at the Γ point and the TA phonon branch, considered highly anharmonic in previous studies, differ significantly between the harmonic approximation and the SCPH+B calculation, with the harmonic approximation predicting smaller frequencies. The potential energy surface of the A_{2u} phonon is no longer a quadratic function and is well described with considering functions up to the fourth order, as in Fig. 4. Table III summarizes the Γ point phonon frequencies. For the A_{2u} and E_u^1 modes, the negative frequency shift by the bubble self-energy and the positive frequency shift by the loop self-energy cancel each other out, resulting in about 50 cm^{-1} positive frequency shift. The A_{2u} phonon frequency within the harmonic approximation is 139 cm^{-1}, which rises to 220 cm^{-1} by SCPH. The

TABLE II: calculated Born effective charge tensors Z of the Ti atom at $(0,0,0)$ and the O atom at $(u,u,0)$.

	Ti			O		
	Z_{xx}	Z_{xy}	Z_{zz}	Z_{xx}	Z_{xy}	Z_{zz}
LDA	6.34	−1.01	7.66	−3.17	1.81	−3.83
r^{2}SCAN	5.96	−0.97	7.27	−2.94	1.71	−3.60

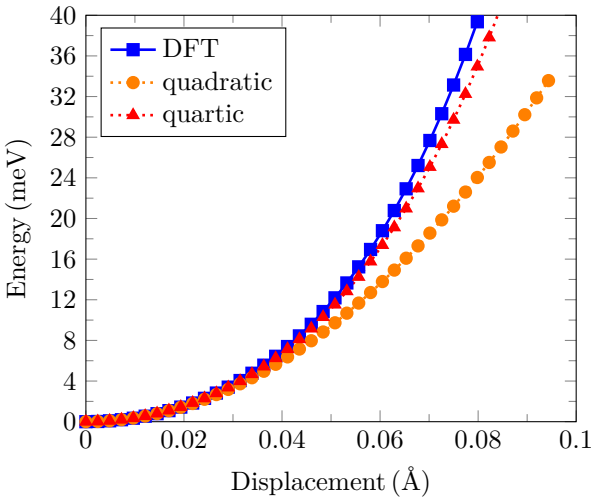

FIG. 4: Frozen phonon potential (blue) of A_{2u} mode with x axis being the displacement of the Ti atoms. The quartic component (red) describes the DFT potential well, while the harmonic component (orange) deviates from the potential.

frequency decreases to 179 cm^{-1} when the bubble self-energy is considered with SCPH+B. The contribution of the anharmonic terms reache 29%. Similarly, the E_u^1 phonon frequency is 133 cm^{-1} for the harmonic approximation, 210 cm^{-1} for SCPH, and 189 cm^{-1} for SCPH+B. Phonon frequencies are also calculated from a usual perturbative approach (abbreviated as non-SC) for r^{2}SCAN as $\omega = \omega_0 + \Delta\omega^{\mathrm{T}} + \Delta\omega^{\mathrm{B}} + \Delta\omega^{\mathrm{L}}$. The non-SC frequencies differ largely from the SCPH+B frequencies in the A_{2u} and E_u^1 phonons. In the A_{2u} phonon mode, we obtained $\Delta\omega^{\mathrm{B}} = -78$ and $\Delta\omega^{\mathrm{L}} = 144$, which are too large to be handled within perturbation theory. This calculation shows that neither the harmonic approximation nor the perturbation method suffices for optical properties, where an accurate estimation of the optical phonon frequencies at the Γ point is necessary.

Figure 3b demonstrates a good agreement between LDA and r^{2}SCAN throughout the Brillouin zone. However, the LDA calculation overestimates the A_{2u} phonon at the Γ point. The underestimation of the lattice constants of LDA may cause the overestimation of the A_{2u} phonon, as the A_{2u} phonon is sensitive to lattice constants [14]. To clarify this point, we have performed the SCPH+B calculation with LDA using the experimental lattice constants. The resultant frequency of the A_{2u} phonon was 146 cm^{-1} , which underestimates the experimental value by 15%. This result shows that the A_{2u} mode is sensitive to the lattice constant even at the level of anharmonic phonon calculations. For the LO phonons, the LDA results overestimate the E_u^3 phonon frequency, the cause of which is larger Born effective charges by LDA than that by r^{2}SCAN. As r^{2}SCAN gives better results than LDA, all the following calculations are based on r^{2}SCAN.

TABLE III: Comparison of the computed mode frequencies (in cm^{-1}) at the Γ point with various experimental data at room temperature. The results from the harmonic approximation (harm), SCPH and SCPH+B are shown for both LDA and r^{2}SCAN at 300 K, while a usual perturbation calculation (non-SC) are shown only for r^{2}SCAN.

	LDA			r^{2}SCAN				neutron [12]	Raman [47]	FPSQ [10]
	harm	SCPH	SCPH+B	harm	SCPH	SCPH+B	non-SC	IR [48]		
					Raman					
A_{1g}	612.5	620.8	616.6	599.8	613.1	613.3	627.1	610	612	-
A_{2g}	395.0	424.0	413.7	456.5	432.9	451.8	458.9	NF[1]	NF	-
B_{1g}	134.7	121.9	116.6	146.5	143.0	138.9	139.1	142	143	-
B_{2g}	817.5	818.2	817.2	809.6	814.4	821.8	831.4	824	826	-
E_g	464.3	476.0	467.5	434.4	463.1	431.5	429.0	445	447	-
					non-active					
B^1_{1u}	108.1	149.6	140.2	103.2	141.0	130.0	159.5	113	-	-
B^2_{1u}	417.9	414.8	413.8	398.4	420.7	411.7	421.8	406	-	-
					TO					
A_{2u}	147.8	227.9	198.0	138.5	210.1	179.4	210.6	172.6	167	172.3
E^1_u	149.0	216.8	202.0	132.7	203.6	186.9	238.4	189	183	188.6
E^2_u	384.3	394.6	386.5	378.8	382.1	374.9	374.3	374	388	379.3
E^3_u	489.0	504.7	492.5	495.7	513.1	500.1	495.0	494	500	500.5
					LO					
A_{2u}	843.9	861.5	854.2	784.9	800.6	793.1	805.2	NF	811	796.5
E^1_u	354.6	362.7	354.0	364.5	364.9	356.9	360.0	375	373	365.7
E^2_u	439.1	447.3	436.8	445.5	455.6	443.9	445.7	428	458	444.9
E^3_u	882.8	904.9	904.9	815.1	836.0	830.7	851.4	842	806	829.6

[1] NF=not found.

Finally, we calculated the temperature dependence of the static dielectric constant $\epsilon^0 \equiv \epsilon(\omega = 0)$, which directly reflects the effect of the phonon frequency shift with temperature. Figure 5 compares the calculated temperature dependence of ϵ^0_x and ϵ^0_z with the experimental data [3]. Both ϵ^0_x and ϵ^0_z increase with lowering temperatures due to a decrease in the phonon frequencies. In particular, ϵ^0_z increases up to 250 at $T = 0$ because of the strong temperature dependence of the A_{2u} phonon frequency. The SCPH+B calculation well reproduced experimental values for ϵ^0_x. For ϵ^0_z, on the other hand, the tendency to increase is reproduced, but the value at $T = 0$ is 169, which is only 70% of the experimental value. In fact, the frequency of the A_{2u} mode at $T = 0$ is 167 cm^{-1} in the SCPH+B calculation, compared to 140 cm^{-1} for the experimental value [12], which indicates that the zero-point vibration is very large. This could be improved by using more acurate functionals like hybrid functionals.

C. phonon linewidth

We calculated the frequency-independent linewidths of the four phonon modes involved in the dielectric function in two ways as

$$\gamma^{\mathrm{SCPH+B}} = 2\,\mathrm{Im}\,\Sigma[G^{\mathrm{SCPH+B}}](\omega = \Omega^{\mathrm{SCPH+B}}) \quad (19)$$

$$\gamma^{\mathrm{non-SC}} = 2\,\mathrm{Im}\,\Sigma[G^{\mathrm{harm}}](\omega = \omega^{\mathrm{harm}}). \quad (20)$$

As mentioned in Sec. II B, while the latter (non-SC) is a usual perturbative calculation, the former uses the SCPH+B phonon frequencies. Table IV shows that the Non-SC linewidths are overestimated significantly, whereas the SCPH+B calculations agree better with the FPSQ data [10], which is determined by fitting experimental reflectivity data to the FPSQ model. It indicates that the calculation of linewidth requires accurate determination of phonon frequencies, including anharmonicity, as pointed out by Fu et al. [23]. Discrepancies are observed in the E^1_u and A_{2u} TO modes with relatively high frequencies, which could be improved by incorporating higher-order diagrams. We also found that self-energies from the four-phonon scattering give a non-

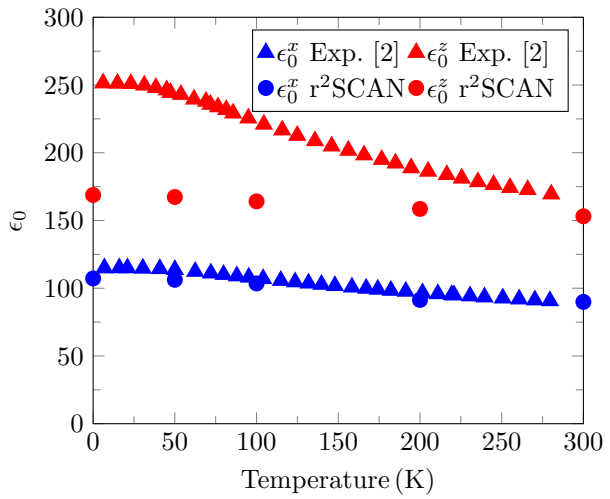

FIG. 5: Temperature dependence of the static dielectric constant. The triangular dots show the experimental values and the circular dots show the results from the SCPH+B calculations.

negligible contribution in the A_{2u} and E_u^1 modes. Such phenomena have been observed in other materials [30].

D. dielectric function

Figure 6a shows the calculated imaginary part of dielectric function together with experimental data. The blue line represents the SCPH+B calculation, while the cyan dashed line represents the non-SC calculation,

TABLE IV: Calculated linewidth (cm^{-1}) of IR-active phonon modes at 300 K together with the experimental parameters fitted with the FPSQ model. The contributions from the bubble diagram, from the 4ph diagram and the sum of the two are shown for both non-SC and SCPH+B results.

	non-SC			SCPH+B			FPSQ [10]
	bubble	4ph	total	bubble	4ph	total	
				TO			
E_u^1	21.2	69.9	91.1	8.54	7.95	16.4	14.7 ± 8.0
E_u^2	40.7	7.09	47.8	14.5	1.81	16.2	19.3 ± 2.8
E_u^3	28.3	11.6	39.9	12.6	3.47	16.0	22.4 ± 3.1
A_{2u}	29.3	51.8	81.1	16.3	9.57	25.7	20.0 ± 10.2
				LO			
E_u^1	13.8	2.71	16.5	7.12	0.97	8.09	8.8 ± 1.8
E_u^2	24.3	8.43	32.7	11.7	2.33	14.0	18.4 ± 2.2
E_u^3	33.0	8.39	41.4	22.6	3.88	26.5	43.9 ± 5.6
A_{2u}	22.8	7.58	30.4	12.6	3.62	16.2	46.4 ± 5.3

TABLE V: Positions of additional peaks (cm^{-1}). $\epsilon_{x,1}$ is for ϵ_{xx} and $\epsilon_{z,1}$ is for ϵ_{zz}.

Mode	r^{2}SCAN	FPSQ [8]	FPSQ [10]
$\epsilon_{x,1}$	563	585	556 ± 5
$\epsilon_{z,1}$	598	592	587 ± 12

where harmonic phonon frequencies are used, and the frequency-dependent self-energy is calculated as

$$\Sigma^{\text{non-SC}}(\omega) = \text{Im}\,\Sigma^{\text{B}}[G^{\text{harm}}] + \Sigma^{\text{4ph}}[G^{\text{harm}}]. \quad (21)$$

The maximum values of the imaginary part of ϵ_{xx} and ϵ_{zz} reach 785 and 932, respectively, which are due to the E_u^1 and A_{2u} phonons with large mode-oscillator strength of $S(E_u^1) = 1.87\,e^2/u$ and $S(A_{2u}) = 6.12\,e^2/u$, respectively. It is because the positively charged Ti ions and negatively charged O ions move in opposite directions in the A_{2u} and E_u^1 phonons, as shown in Fig. 1. On the other hand, in the E_u^2 and E_u^3 phonons, the two Ti atoms move in opposite directions, so the mode oscillator strength is much smaller. The renormalization of phonon eigenvectors by SCPH is negligible, and it is the phonon frequencies and self-energies that affect the calculation results of dielectric properties. The SCPH+B calculations agree remarkably well with experimental values, whereas the non-SC calculations failed to reproduce experimental data, especially in the A_{2u} and E_u^1 peaks.

Figure 6b shows the reflectivity R in x and z directions calculated using Eq. (5). For the x direction, the dip due to the E_u^2 phonon ($380\,cm^{-1}$) is shallower than the experimental data, whereas the dip due to the E_u^1 and E_u^3 phonons (bellow $200\,cm^{-1}$ and $450\,cm^{-1}$) are in good agreement with experiment. The SCPH+B calculations are overall in better agreement with experiment than the non-SC calculations.

To examine the importance of the frequency dependence of the self-energy, dielectric functions in the logarithm scale are shown in Fig. 7, together with the experimental data from Schoche [10]. The dielectric functions ϵ_{xx} and ϵ_{zz} have one peak each at about $600\,cm^{-1}$, which is not the position of any IR-active phonon frequency at the Γ point. Several experiments [7, 10] reported that adding these additional peaks to the FPSQ model improved agreement with experimental data. The peak positions are listed in Table V together with these experimental data.

Possible origins of these peaks, such as lattice defects, have been argued, but the causes are still unclear [10]. The imaginary part of frequency-dependent self-energies can explain these peaks. The frequency dependence of the 4ph self-energy is not so strong, whereas the bubble self-energy has strong frequency dependence in rutile TiO_2. Figure 8 shows the bubble self-energies of the E_u^3 and A_{2u} phonons, which contribute to ϵ_{xx} and ϵ_{zz}, respectively, with vertical dotted lines corresponding to the positions of additional peaks. The bubble self-energies

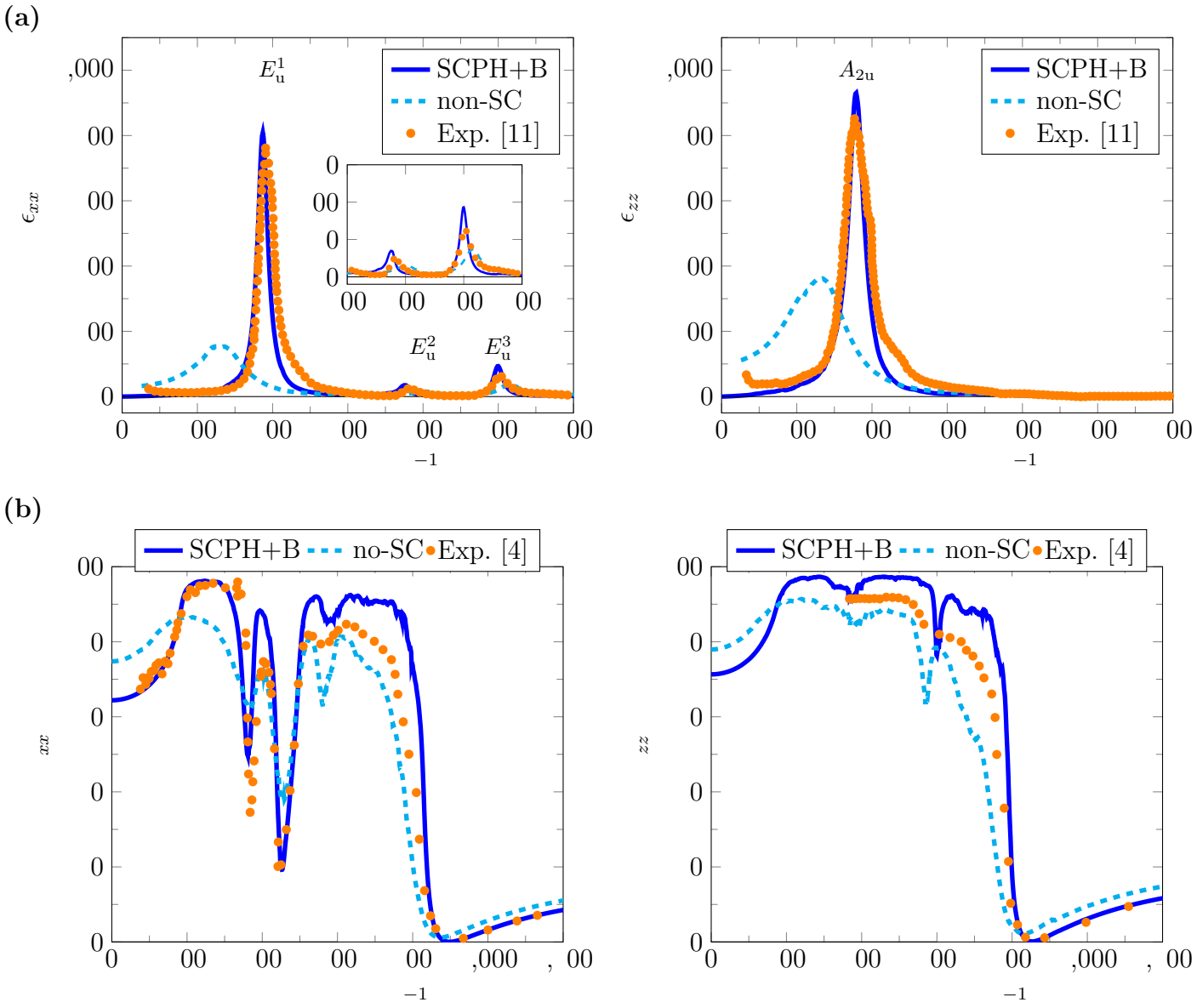

FIG. 6: (a) Calculated imaginary part of dielectric functions ϵ_{xx} (left) and ϵ_{zz} (right) from SCPH+B (solid blue lines) and harmonic approximation (dashed cyan lines) with experimental data at room temperature [11] (orange open circles). The TO phonons corresponding to the peaks are marked. (b) Calculated reflectivity from SCPH+B (solid blue lines) with experimental data at room temperature [4].

also have peaks at the positions of the additional peaks. We ascribe, therefore, the bubble self-energy to the additional peaks.

When the bubble diagram is taken into account, the dielectric function, and thus the Green's function, has peaks at a certain frequency ω when the two phonons with frequencies (ω_1, ω_2) satisfy the relation $\omega = \omega_1 \pm \omega_2$ and $\boldsymbol{q}_1 \pm \boldsymbol{q}_2 = \boldsymbol{0}$. The positive sign corresponds to phonon emission, and the negative sign to phonon absorption. Such phonon pairs can be specified by the two-phonon density of states (TDOS), which is defined as follows,

$$\mathrm{TDOS}_{\pm}(\omega, \boldsymbol{q}) = \frac{1}{N_q} \sum_{\substack{(\boldsymbol{q}_1, j_1) \\ (\boldsymbol{q}_2, j_2)}} \delta(\omega \pm \omega_{\boldsymbol{q}_1 j_1} - \omega_{\boldsymbol{q}_2 j_2}) \delta_{\boldsymbol{q} \pm \boldsymbol{q}_1, \boldsymbol{q}_2 + \boldsymbol{G}}. \tag{22}$$

Here $\boldsymbol{G}$ is a reciprocal lattice vector, and N_q is the number of q points in the summation. Figure 9 presents the calculated $\mathrm{TDOS}(\omega, \boldsymbol{q} = \boldsymbol{0})$ with a $15 \times 15 \times 15$ q points grid, in which TDOS for the emission process has a considerable value at around 600 cm^{-1}. Furthermore, from Fig. 3, phonon DOS peaks at around 115, 210, 300, 398, and 455 cm^{-1}, of which the 115 cm^{-1} one is due

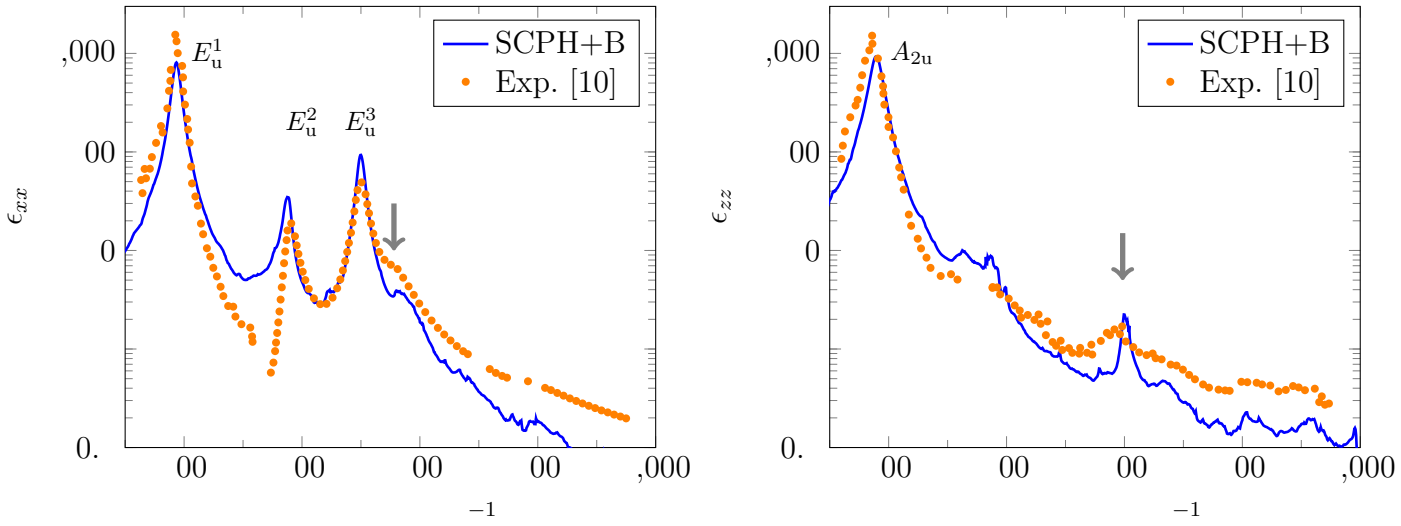

FIG. 7: Calculated imaginary part of dielectric functions with experimental data from Schoche [10] in a logarithm scale. Both ϵ_{xx} and ϵ_{zz} have a peak at about $600\,\mathrm{cm}^{-1}$, which does not belong to any IR-active phonon frequency, and these peaks are indicated by the gray arrows.

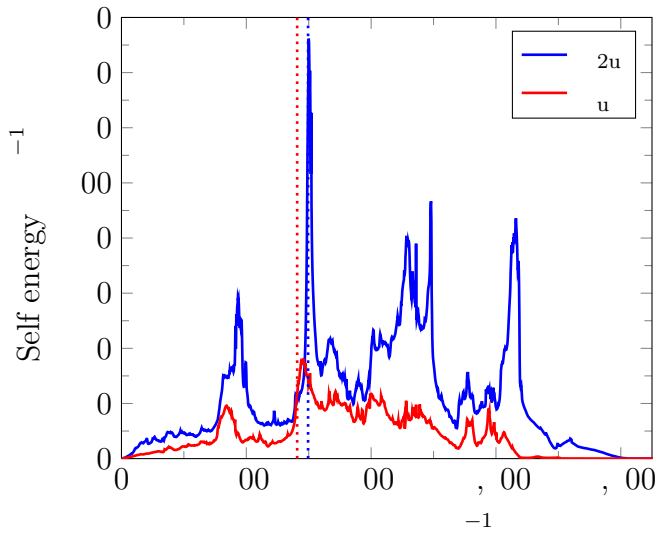

FIG. 8: Calculated imaginary part of frequency dependent bubble self-energy of A_{2u} (blue) and E_u^3 (red) modes. Blue and red vertical lines represent the additional peaks for ϵ_{zz} and ϵ_{xx}, respectively.

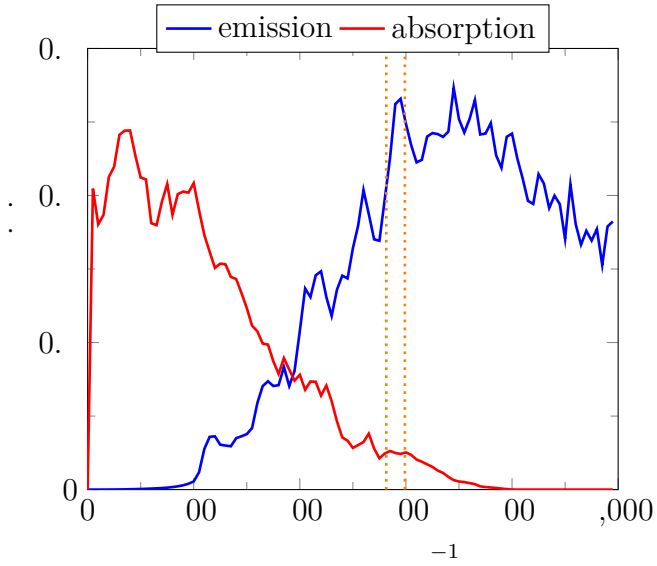

FIG. 9: Calculated $\mathrm{TDOS}_{\pm}(\omega, \boldsymbol{q} = \mathbf{0})$ for absorption (red) $\omega = \omega_1 - \omega_2$ and emission (blue) $\omega = \omega_1 + \omega_2$. Red vertical lines represent the positions of additional peaks.

to acoustic phonons and the others are due to optical phonons. Therefore, it is concluded that the $600\,\mathrm{cm}^{-1}$ additional peak is created by the emission process of the pairs $(115\,\mathrm{cm}^{-1}, 455\,\mathrm{cm}^{-1})$, $(210\,\mathrm{cm}^{-1}, 398\,\mathrm{cm}^{-1})$ and $(300\,\mathrm{cm}^{-1}, 300\,\mathrm{cm}^{-1})$. Notably, the first pair emission process, involving the acoustic modes, is contributed by phonons with non-zero wave numbers, which can not be detected via single phonon processes by optical probes that are sensitive to Γ point phonons.

E. functional dependence

We have seen that the combination of r^{2}SCAN and SCPH+B gives generally good results for phonon frequencies and dielectric properties, meanwhile the lowest phonon branch (B_{1u}^1) in Fig. 3a and the temperature-dependent dielectric constant ϵ_0^z in Fig. 5 are not in good agreement with experiment. To investigate the causes of these discrepancies, we also performed SCPH+B calculations using the PBEsol functional [52]. The results are summarized in Appendix B. Although the PBEsol func-

tional predicts the lattice constants well in Table BI, it underestimates the overall phonon frequencies, which is well known for the GGA family in the rutile TiO_2 [14, 53]. However, its description of the B^1_{1u} branch is superior to that of LDA and r^{2}SCAN as in Fig. B1. This result implies that the B^1_{1u} phonon also highly depends on functionals like the A_{2u} phonon.

The calculated behavior of ϵ^z_0 with PBEsol at low temperatures in Fig. B2 shows better agreement with experiment than r^{2}SCAN. The r^{2}SCAN calculation gives a frequency of A_{2u} of $167\,\mathrm{cm}^{-1}$ at $T = 0$, whereas PBEsol yields $143\,\mathrm{cm}^{-1}$, close to the experimental value ($140\,\mathrm{cm}^{-1}$ [12]). This is why the large ϵ^z_0 value at low temperature is well reproduced in the PBEsol calculation.

We have here seen that some physical quantities are strongly dependent on functionals. These problems could be cured by further functional improvements.

IV. CONCLUSIONS

We studied the infrared spectra of rutile TiO_2 using first-principles (DFT) calculations and lattice dynamics calculations. The calculation of phonon frequencies was performed using the SCPH+B theory, a self-consistent anharmonic phonon theory [Fig. 3]. The SCPH+B calculation very well described the E^1_u and A_{2u} phonon frequencies, which were greatly underestimated in the harmonic approximation. We showed that the anharmonicity in these modes is too strong to treat in a perturbative approach, and self-consistent treatment is essential for accurately describing phonon frequencies. We also compared the LDA and r^{2}SCAN results, finding that the r^{2}SCAN functional is more predictive, especially in describing the A_{2u} mode.

Phonon linewidths were calculated using both the perturbation theory (non-SC) and the SCPH+B theory. They were significantly overestimated in the non-SC calculation, as suggested by Fu et al. [23]. We also found that the contribution from the 4ph self-energy is non-negligible at 300 K. The SCPH+B dielectric function showed good agreement with experimental values. Furthermore, the additional peaks at around $600\mathrm{cm}^{-1}$ pointed out in the previous experiments can be attributed to the two phonon emission process included in the frequency-dependent bubble diagram, which shows the importance of the frequency dependence of phonon self-energies in accurately calculationg the dielectric function. We expect the presented approach to be useful in predicting the dielectric properties of other materials.

ACKNOWLEDGMENTS

This research was funded by a JST-Mirai Program Grant Number JPMJMI20A1, a MEXT Quantum Leap Flagship Program (MEXT Q-LEAP) grant number JPMXS0118067246, Japan, and JSR Corporation via JSR-UTokyo Collaboration Hub, CURIE. T.T. is partially supported by JSPS KAKENHI Grant No. 21K03424. The computations in this study have been done using the facility of the Supercomputer Center, the Institute for Solid State Physics, the University of Tokyo.

Appendix A: Derivation of the Cowley equation

We review the derivation of the Cowley equation (3). Consider a supercell with L unit lattices and impose periodic boundary condition. The coordinates of the atoms are denoted by $\boldsymbol{R}$. If the atomic displacements from the equilibrium positions $\boldsymbol{R}_0$ are small compared with the interatomic distance, the dipole moment of the interacting atomic system can be expanded in a power series of the displacements $\boldsymbol{u}(l\kappa) = \boldsymbol{R}(l\kappa) - \boldsymbol{R}_0(l\kappa)$ as

$$\delta \boldsymbol{M} = \boldsymbol{M}_1 + \boldsymbol{M}_2 + \boldsymbol{M}_3 + \cdots \tag{A1}$$

where the α component of $\boldsymbol{M}_n$ is

$$\begin{aligned} M_{n,\alpha} =& \frac{1}{n!} \sum_{l_1\kappa_1\mu_1} \cdots \sum_{l_n\kappa_n\mu_n} M^{l_1\kappa_1, l_2\kappa_2, \cdots l_n\kappa_n}_{\alpha,\mu_1\cdots\mu_n} \\ & \times u_{\mu_1}(l_1\kappa_1) u_{\mu_2}(l_2\kappa_2) \cdots u_{\mu_n}(l_n\kappa_n) \end{aligned} \tag{A2}$$

Here, μ and α are the indices of Cartesian coordinates, and $u_\mu(l\kappa)$ is the displacement of the atom κ in the l th cell. The coefficient $M^{l_1\kappa_1, l_2\kappa_2, \cdots l_n\kappa_n}_{\alpha,\mu_1\cdots\mu_n}$ is the nth-order derivative of $\boldsymbol{M}$ with respect to atomic coordinates as

$$M^{l_1\kappa_1, \cdots, l_n\kappa_n}_{\alpha,\mu_1\cdots\mu_n} = \frac{\partial M_\alpha}{\partial u_{\mu_1}(l_1\kappa_1) \cdots \partial u_{\mu_n}(l_n\kappa_n)}. \tag{A3}$$

Thus, the first-order coefficient is the Born effective charge as $M_{\alpha,\beta}(l\kappa) = Z^*_{\kappa,\alpha\beta}$. From the periodic boundary condition, the value of the quantity does not change when the same number is added to the indices of all cells as

$$M^{l_1\kappa_1, \cdots l_n\kappa_n}_{\alpha,\mu_1\cdots\mu_n} = M^{0\kappa_1, l_2 - l_1\kappa_2, \cdots l_n - l_1\kappa_n}_{\alpha,\mu_1\cdots\mu_n}. \tag{A4}$$

Next, we introduce the complex normal coordinate Q_q, with which the atomic displacement is expressed as

$$u_\mu(l\kappa) = \frac{1}{\sqrt{L m_\kappa}} \sum_q Q_q e_{\mu\kappa}(q) e^{i\boldsymbol{q}\cdot\boldsymbol{r}_l}, \tag{A5}$$

By substituting Eq. (A5) for Eq. (A2) and using Eq. (A4), we obtain $\boldsymbol{M}_n$ expressed in terms of the normal coordinate as follows,

$$\boldsymbol{M}_n = \frac{1}{n!} \frac{L}{L^{n/2}} \sum_{q_1,\cdots,q_n} \Delta(\boldsymbol{q}_1 + \cdots \boldsymbol{q}_n) \boldsymbol{M}(q_1, \cdots, q_n) Q_{q_1} \cdots Q_{q_n}, \tag{A6}$$

where

$$\boldsymbol{M}(q_1,\cdots,q_n)=\sum_{\kappa_1\mu_1}\cdots\sum_{l_n\kappa_n\mu_n}\boldsymbol{M}^{0\kappa_1,l_2\kappa_2,\cdots,l_n\kappa_n}_{\mu_1\cdots\mu_n}\times\frac{1}{\sqrt{m_{\kappa_1}\cdots m_{\kappa_n}}}e_{\mu_1}(q_1,\kappa_1)\cdots e_{\mu_n}(q_n,\kappa_n)\times\exp\left(i(\boldsymbol{q}_2\cdot\boldsymbol{r}_{l_2}+\cdots+\boldsymbol{q}_n\cdot\boldsymbol{r}_{l_n})\right). \tag{A7}$$

$\Delta(\boldsymbol{q})$ takes the value 1 only when $\boldsymbol{q}$ is the reciprocal lattice vector and 0 otherwise. Therefore, the summation in first-order expansion is restricted to $\boldsymbol{q}_1=\boldsymbol{0}$, and that of the second-order expansion is restricted to $\boldsymbol{q}_2=-\boldsymbol{q}_1$.

When phonon frequencies of all phonon modes are real in the entire Brillouin zone, one may further transform Eq. (A7) into a second quantization representation by using $Q_q=(\hbar/2\omega_q)^{1/2}A_q$ with $A_q=b_q+b_q^\dagger$ being the displacement operator.

$$\boldsymbol{M}_n=\frac{L}{n!}\left(\frac{\hbar}{2L}\right)^{n/2}\sum_{q_1,\cdots,q_n}\Delta(\boldsymbol{q}_1+\cdots+\boldsymbol{q}_n)\times\frac{\boldsymbol{M}(q_1,\cdots,q_n)}{\sqrt{\omega_{q_1}\cdots\omega_{q_n}}}A_{q_1}\cdots A_{q_n}, \tag{A8}$$

When an external electric field $\boldsymbol{E}(t)=\boldsymbol{E}_0e^{-i\omega t+\delta t}$ is applied to the system, the interaction is represented by the Hamiltonian as

$$H_I=-\boldsymbol{M}\cdot\boldsymbol{E}(t). \tag{A9}$$

According to the linear response theory, the expectation value of the polarization $\boldsymbol{P}=\boldsymbol{M}/v_0$ of the system is

$$\bar{P}_\alpha(t)=\frac{1}{v_0}G^R(M_\alpha,\boldsymbol{M},\omega)\cdot\mathbf{E}(t), \tag{A10}$$

where $G^R(A,B,\omega)$ is the retarded Green's function for operators A and B. By using the fact that the polarization and the electric field are connected by the dielectric susceptibility $\boldsymbol{\chi}$ as $P_\alpha=\chi_{\alpha\beta}\epsilon_0E_\beta$ and that the dielectric function $\boldsymbol{\epsilon}$ in the IR region is the sum of the phonon contribution $\boldsymbol{\chi}$ and the electron contribution $\boldsymbol{\epsilon}^\infty$ as $\epsilon_{\alpha\beta}=\epsilon^\infty_{\alpha\beta}+\chi_{\alpha\beta}$, the dielectric function can be written as

$$\epsilon_{\alpha\beta}(\omega)=\epsilon^\infty_{\alpha\beta}+\frac{1}{v_0}G^R(M_\alpha,M_\beta,\omega). \tag{A11}$$

Substituting Eq. (A8) into Eq. (A11), the lowest order contribution of the dielectric function, as shown in Fig. A1, is

$$\epsilon_{\alpha\beta}(\omega)=\epsilon^\infty_{\alpha\beta}+\frac{1}{v_0}\sum_{jj'}\frac{\hbar}{2}\frac{M(\mathbf{0}j)M(\mathbf{0}j')}{\sqrt{\omega_{\mathbf{0}j}\omega_{\mathbf{0}j'}}}G^R(A_{\mathbf{0}j},A_{\mathbf{0}j'},\omega)=\epsilon^\infty_{\alpha\beta}+\frac{1}{v_0}\sum_{(\mathbf{0},j)}\frac{S^j_{\alpha\beta}}{(\omega_{\mathbf{0}j})^2-\omega^2-2\omega_{\mathbf{0}j}\Sigma_{\mathbf{0}j}(\omega)}. \tag{A12}$$

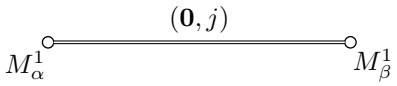

FIG. A1: The lowest order of the dielectric function. The double line represents the full-phonon Green's function.

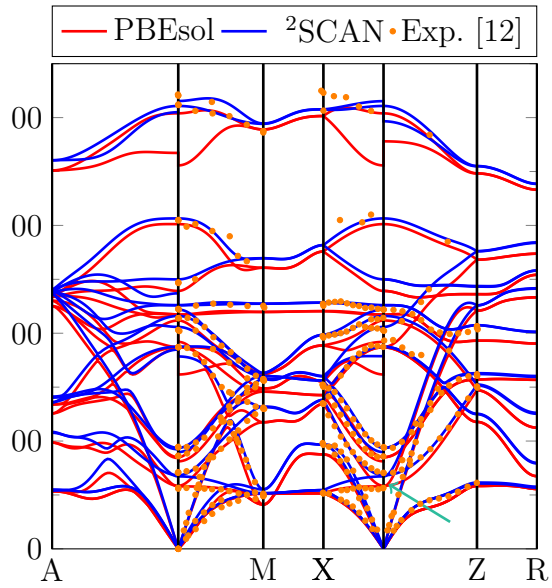

FIG. B1: The SCPH+B band structure with r^{2}SCAN (blue) and PBEsol (red) functional. The green arrow indicate the B_{1u} mode, which is overestimated in the r^{2}SCAN functional.

Appendix B: The results of the PBEsol functional

We summarized the calculation results of the PBEsol functional. Table BI shows the optimized lattice constants, and Table BII shows the Born effective charges obtained from PBEsol. Figure B1 shows the phonon dispersion spectrum along the high-symmetry points in the first Brillouin zone at 300 K with non-analytic term correction, together with inelastic neutron scattering results from Traylor [12] (orange dots), while Table BIII shows the phonon frequencies at the Γ point. Figure B2 shows the temperature-dependent dielectric constants from PBEsol.

TABLE BI: calculated lattice constants with PBEsol.

	a (Å)	c (Å)	u	c/a	v_0 (Å^3)
PBEsol	4.595	2.942	0.3044	0.640	62.12
Exp. 300 K [46]	4.593	2.959	0.3048	0.644	62.42
Exp. 15 K [46]	4.587	2.954	0.3047	0.644	62.15

TABLE BII: calculated Born effective charge tensors Z of the Ti atom at $(0,0,0)$ and the O atom at $(u,u,0)$. $Z_{xx}=Z_{yy}$, $Z_{yz}=Z_{zy}$, and Z_{zz} are shown considering the symmetry.

	Ti			O		
	Z_{xx}	Z_{xy}	Z_{zz}	Z_{xx}	Z_{xy}	Z_{zz}
PBEsol	4.26	−1.13	7.64	−3.16	1.80	−3.85

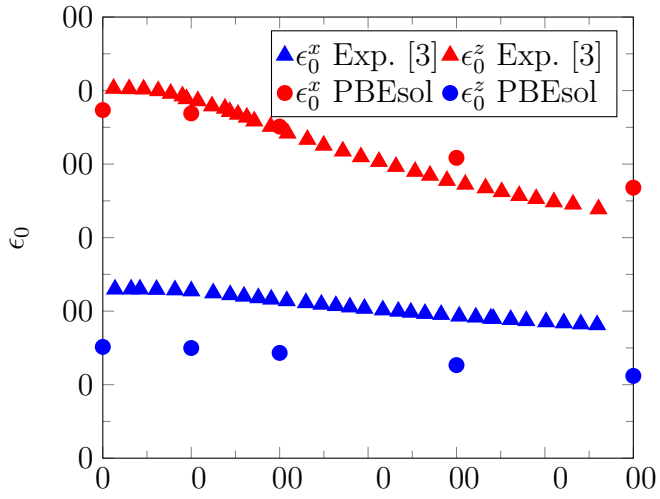

FIG. B2: Temperature dependence of the static dielectric constant. The triangular dots show the experimental values and the circular dots show the results from the SCPH+B calculations.

TABLE BIII: Comparison of the computed mode frequencies (in cm^{-1}) at the Γ point with experimental data at room temperature. The results from the harmonic approximation (harm), SCPH and SCPH+B are shown at 300 K.

	PBEsol			neutron [12]
	harm	SCPH	SCPH+B	
		Raman		
A_{1g}	590.2	601.3	602.4	610
A_{2g}	415.4	424.1	423.6	NF[1]
B_{1g}	140.8	119.8	117.0	142
B_{2g}	793.5	802.8	807.9	824
E_g	447.4	444.8	434.5	445
		non-active		
B_{1u}^1	77.9	131.9	115.9	113
B_{1u}^2	374.4	387.4	374.3	406
		TO		
A_{2u}	71.0	202.7	162.4	172.6
E_u^1	98.8	187.0	169.9	189
E_u^2	367.3	379.2	373.8	374
E_u^3	478.0	493.0	478.4	494
		LO		
A_{2u}	741.7	765.6	756.0	NF
E_u^1	327.3	334.5	323.5	375
E_u^2	378.0	390.9	383.9	428
E_u^3	695.5	719.4	711.3	842

[1] NF=not found.

[1] S. K. Kim, W.-D. Kim, K.-M. Kim, C. S. Hwang, and J. Jeong, Appl. Phys. Lett. **85**, 4112 (2004).
[2] J. R. DeVore, J. Opt. Soc. Am., JOSA **41**, 416 (1951).
[3] R. A. Parker, Phys. Rev. **124**, 1719 (1961).
[4] W. G. Spitzer, R. C. Miller, D. A. Kleinman, and L. E. Howarth, Phys. Rev. **126**, 1710 (1962).
[5] A. S. Barker and M. Tinkham, J. Chem. Phys. **38**, 2257 (1963).
[6] G. A. Samara and P. S. Peercy, Phys. Rev. B **7**, 1131 (1973).
[7] F. Gervais and B. Piriou, J. Phys. C: Solid State Phys. **7**, 2374 (1974).
[8] F. Gervais and B. Piriou, Phys. Rev. B **10**, 1642 (1974).
[9] N. Matsumoto, T. Hosokura, K. Kageyama, H. Takagi, Y. Sakabe, and M. Hangyo, Jpn. J. Appl. Phys. **47**, 7725 (2008).
[10] S. Schöche, T. Hofmann, R. Korlacki, T. E. Tiwald, and M. Schubert, Journal of Applied Physics **113**, 164102 (2013).
[11] K. Kanehara, T. Hoshina, H. Takeda, and T. Tsurumi, Journal of the Ceramic Society of Japan **123**, 303 (2015).
[12] J. G. Traylor, H. G. Smith, R. M. Nicklow, and M. K. Wilkinson, Phys. Rev. B **3**, 3457 (1971).
[13] C. Lee and X. Gonze, Phys. Rev. B **49**, 14730 (1994).
[14] B. Montanari and N. M. Harrison, Chemical Physics Letters **364**, 528 (2002).
[15] B. Montanari and N. M. Harrison, J. Phys.: Condens. Matter **16**, 273 (2004).
[16] R. Sikora, Journal of Physics and Chemistry of Solids **66**, 1069 (2005).
[17] P. D. Mitev, K. Hermansson, B. Montanari, and K. Refson, Phys. Rev. B **81**, 134303 (2010).

[18] B. Lee, C.-k. Lee, C. S. Hwang, and S. Han, Current Applied Physics International Conference on Electronic Materials, **11**, S293 (2011).
[19] A. Grünebohm, C. Ederer, and P. Entel, Phys. Rev. B **84**, 132105 (2011).
[20] B. Wehinger, A. Bosak, and P. T. Jochym, Phys. Rev. B **93**, 014303 (2016).
[21] Y. Zhang, J. W. Furness, B. Xiao, and J. Sun, J. Chem. Phys. **150**, 014105 (2019).
[22] P. Torres and R. Rurali, J. Phys. Chem. C **123**, 30851 (2019).
[23] B. Fu, G. Tang, and A. J. H. McGaughey, Phys. Rev. Materials **6**, 015401 (2022).
[24] O. Hellman, I. A. Abrikosov, and S. I. Simak, Phys. Rev. B **84**, 180301 (2011).
[25] T. Tadano and S. Tsuneyuki, Phys. Rev. B **92**, 054301 (2015).
[26] T. Tadano and S. Tsuneyuki, J. Phys. Soc. Jpn. **87**, 041015 (2018).
[27] T. Tadano and W. A. Saidi, Phys. Rev. Lett. **129**, 185901 (2022).
[28] A. van Roekeghem, J. Carrete, S. Curtarolo, and N. Mingo, Phys. Rev. Materials **4**, 113804 (2020).
[29] W. I. Choi, J. S. An, I. Jang, and D. S. Kim, Current Applied Physics **29**, 78 (2021).
[30] X. Yang, T. Feng, J. S. Kang, Y. Hu, J. Li, and X. Ruan, Phys. Rev. B **101**, 161202 (2020).
[31] Z. Tong, X. Yang, T. Feng, H. Bao, and X. Ruan, Phys. Rev. B **101**, 125416 (2020).
[32] G. Fugallo, B. Rousseau, and M. Lazzeri, Phys. Rev. B **98**, 184307 (2018).
[33] R. Cowley, Advances in Physics **12**, 421 (1963).
[34] M. Born, K. Huang, and M. Lax, American Journal of Physics **23**, 474 (1955).
[35] X. Gonze and C. Lee, Phys. Rev. B **55**, 10355 (1997).
[36] R. G. Della Valle and P. Procacci, Phys. Rev. B **46**, 6141 (1992).
[37] C. M. B. Henderson, K. S. Neuhoff, and A. R. Lennie, The Open Mineralogy Journal **3** (2009).
[38] G. Kresse and J. Furthmüller, Phys. Rev. B **54**, 11169 (1996).
[39] J. P. Perdew and A. Zunger, Phys. Rev. B **23**, 5048 (1981).
[40] J. W. Furness, A. D. Kaplan, J. Ning, J. P. Perdew, and J. Sun, J. Phys. Chem. Lett. **11**, 8208 (2020).
[41] G. Kresse and D. Joubert, Phys. Rev. B **59**, 1758 (1999).
[42] J. P. Perdew, A. Ruzsinszky, G. I. Csonka, O. A. Vydrov, G. E. Scuseria, L. A. Constantin, X. Zhou, and K. Burke, Phys. Rev. Lett. **100**, 136406 (2008).
[43] T. Lan, C. W. Li, O. Hellman, D. S. Kim, J. A. Muñoz, H. Smith, D. L. Abernathy, and B. Fultz, Phys. Rev. B **92**, 054304 (2015).
[44] F. Zhou, W. Nielson, Y. Xia, and V. Ozoliņš, Phys. Rev. Lett. **113**, 185501 (2014).
[45] T. Tadano, Y. Gohda, and S. Tsuneyuki, J. Phys.: Condens. Matter **26**, 225402 (2014).
[46] J. K. Burdett, T. Hughbanks, G. J. Miller, J. W. Richardson, and J. V. Smith, J. Am. Chem. Soc. **109**, 3639 (1987).
[47] S. P. S. Porto, P. A. Fleury, and T. C. Damen, Phys. Rev. **154**, 522 (1967).
[48] D. M. Eagles, Journal of Physics and Chemistry of Solids **25**, 1243 (1964).
[49] F. Labat, P. Baranek, C. Domain, C. Minot, and C. Adamo, J Chem Phys **126**, 154703 (2007).
[50] M. Dou and C. Persson, Journal of Applied Physics **113**, 083703 (2013).
[51] T. Lan, X. Tang, and B. Fultz, Phys. Rev. B **85**, 094305 (2012).
[52] In the calculations of the PBEsol functional, which is different from r^{2}SCAN and LDA calculations, 100 structures were randomly generated according to the distribution of the normal coordinate at 500 K for computational stability, with cut-offs for the fifth and sixth orders increased to 10 bohr.
[53] E. Shojaee and M. R. Mohammadizadeh, J. Phys.: Condens. Matter **22**, 015401 (2009).